# Fundamental limit on the heralded single photons' spectral brightness

Tse-Yu Lin,<sup>1</sup> Wei-Kai Huang,<sup>1</sup> Pei-Yu Tu,<sup>1</sup> Yong-Fan Chen,<sup>2</sup> Ite A. Yu<sup>1,3,\*</sup>

<sup>1</sup>Department of Physics and Center for Quantum Science and Technology,

National Tsing Hua University, Hsinchu 30013, Taiwan

<sup>2</sup>Department of Physics, National Cheng Kung University, Tainan 70101, Taiwan

<sup>3</sup>National Center for Excellence in Quantum Information Science and Engineering,

National Tsing Hua University, Hsinchu 30013, Taiwan

#### Abstract

The heralded single photons' (HSPs) spectral brightness (SB) is defined as the generation rate per linewidth. As the generation rate of HSPs gets larger or the photons' linewidth becomes narrower, both of which are desirable in quantum information processing using HSPs, does the SB have a limit? We systematically studied the SB and the cross-correlation function, or equivalently, the signal-to-background ratio. The results in this study provide an answer applicable to all types of HSP sources. The answer relies on a newly defined quantity, the quality factor, which reveals how a HSP source approaches the ideal noise-free one. Furthermore, employing the HSP source based on hot atomic vapor, we achieved an SB of  $(7.0\pm0.3)\times10^5$  pairs/s/MHz and a quality factor of  $0.68\pm0.02$  under the single-photon criterion. Both values are the highest records to date among all kinds of HSP sources.

<sup>\*</sup>Electronic address: yu@phys.nthu.edu.tw

#### I. INTRODUCTION

Single-photon sources are key requirements for long-distance quantum communication protocols. However, producing single photons as carriers of quantum information on demand is not an easy task due to the stochastic nature of their generation process. There are two distinct paths to approaching single-photon sources: (quasi-)deterministic sources employing single emitters and heralded, probabilistic sources employing ensembles of emitters. The latter ones generate time-correlated photon pairs, termed biphotons, at random times. One of the photons is then used as a herald to announce the presence of the other photon, thereby removing the randomness of the generation process. The biphotons are also known as the heralded single photons (HSPs).

Biphotons or HSPs can be generated via the processes of spontaneous parametric down-conversion (SPDC) [1–15] or spontaneous four-wave mixing (SFWM) [16–39] in diverse media such as nonlinear crystals, waveguides, optical fibers, micro-resonators, laser-cooled atom clouds, or heated atomic vapor. Important figures of merit of biphoton sources are their spectral brightness (SB), the signal-to-background ratio (SBR), and the pairing probability (PP). SB is defined as the biphoton generation rate per linewidth. A biphoton source with a higher generation rate can produce information carriers more quickly. Given the finite bandwidths of light-matter interaction, however, a quantum operation can achieve better efficiency with biphotons of a narrower linewidth. Thus, SB has a strong influence on the success rate of quantum operations. On the other hand, SBR represents the peak ratio of the heralded photon number per time bin to the background one in the biphoton wave packet, reflecting the purity of the single photons [40, 41]. This purity impacts the fidelity of quantum operations that utilize these HSPs. A higher SB (or SBR) consistently results in a lower SBR (or SB) [32], and progress has been made in the past decades to optimize either one of them [42–44].

The third, less commonly measured figure of merit, the PP, quantifies the likelihood of having correlated single photons in the heralding and heralded channels and is given by the product of the heralding probabilities of each photon within a pair. This PP indicates the percentages of noise photons, where the noise photons can be single photons due to uncorrelated emissions, correlatively emitted single photons that lose their counterparts in a medium, or laser leakages, etc. When the PP of a biphoton source approaches 1, the

percentages of noise photons in the heralding and heralded channels approach 0, i.e., the source is very close to an ideal noise-free source.

We here define a new quantity, the quality factor, as the product of effective spectral brightness (ESB) and SBR to characterize the combined performance of SB and SBR of a biphoton source. We show that this quality factor is proportional to the PP, where the proportionality is determined by the waveform shape. Even in the limit of negligible background noise, the quality factor accurately accounts for the reduced SBR due to the overlapping of successive photons as the photon generation rate or temproal width increases. Therefore, the quality factor allows one to determine the fundamental limit of a biphoton source's spectral brightness.

This work systematically studied the quality factor of a double- $\Lambda$  SFWM biphoton source with hot atomic vapor. Our study began with an experimental verification of the universal relationship between the quality factor and pairing probability outlined in Eq. (1). Following this, we investigated how various experimental parameters affect the PP, i.e., the product of the heralding probabilities, and provided theoretical interpretations for the observed behaviors. After optimizing various experimental parameters, we achieved a PP of  $0.81\pm0.02$ , i.e., about 90% of the photons, on average, in two detection channels were the paired biphotons. This pairing probability resulted in a quality factor of  $0.68\pm0.02$ , corresponding to, at SBR of  $6.9\pm0.1$ , an ESB of  $(9.8\pm0.4)\times10^4$  (pairs/s)· $\mu$ s or SB of  $(7.0\pm0.3)\times10^5$  pairs/s/MHz, referring to the biphotons collected in polarization-maintained optical fibers.

#### II. QUALITY FACTOR OF A BIPHOTON SOURCE

In the following, we will motivate our definition of the quality factor, Q. Since a HSP or biphoton wave packet's full width at half maximum (FWHM),  $\Delta \tau$ , is proportional to the reciprocal of the biphoton linewidth, the ESB, given by the product of  $\Delta \tau$  and the biphoton generation rate,  $R_b$ , is another way to represent SB, given by  $R_b$  per linewidth. An ESB and its corresponding SB differ by a factor of the order of  $2\pi$ . Consider an ideal biphoton source, which produces only pairs of single photons without any noise. Biphotons of an ideal noise-free source can overlap their wave packets, producing background photons or accidental counts. The accidental count occurs when two detected single photons, one in the heralding channel and the other in the heralded channel, originate from different pairs.

A more significant ESB increases the probability of overlapping wave packets, resulting in a higher background photon count rate or a lower SBR. With the ideal no-noise biphoton source, the value of Q reaches an upper limit, and so does that of ESB or SB under a given SBR.

To understand the relationship between ESB and SBR, we derived a universal formula in Appendix A. To provide clearer physical insight, we show the formula by relating Q or the product of ESB and SBR to the pairing probability, P, of having correlated single photons in heralding and heralded channels as follows:

$$Q \text{ (or ESB} \times \text{SBR)} = C \times P, \tag{1}$$

$$P \equiv h_s h_p, \tag{2}$$

$$P \equiv h_s h_p, \tag{2}$$

$$C \equiv \frac{f(\tau_0) \Delta \tau}{\int_{-\infty}^{\infty} f(\tau) d\tau}, \tag{3}$$

where  $h_s$   $(h_p)$  is the heralding probability, C is a constant depending only on the shape of the biphoton wave packet, and  $f(\tau)$ ,  $\Delta \tau$ , and  $\tau_0$  represent the functional form, temporal FWHM, and peak position of the wave packet. Since we name the two single photons of a biphoton pair as the signal and probe photons,  $h_s = R_b/R_s$  ( $h_p = R_b/R_p$ ) is the heralding probability, using the signal (probe) photon to herald the probe (signal) photon, where  $R_s$  $(R_p)$  is the signal (probe) photon generation rate.

The value of the quality factor Q is between 0 and C, where  $C \leq 1$ . Table III in Appendix A shows the upper limits of Q, i.e., C, under given functional forms. The ideal noise-free HSP or biphoton source has P=1 or a Q value reaching the upper limit. A HSP source with a Q value below C indicates that P is below 1 or, equivalently, it contains noise photons, where the noise photons can be single photons due to uncorrelated emissions, correlatively emitted single photons that lose their counterparts in a medium, or laser leakages, etc. A lower P value represents a higher ratio of noise photons to biphotons. Because of Eq. (1), a HSP source with a lower Q value is farther away from the ideal noise-free one and contains more noise photons. Therefore, the Q value can qualitatively indicate how closely a HSP source approaches an ideal noise-free one.

In the derivation of Eq. (1), we used the approximation of about one heralded photon per successful heralding event. The single-photon criterion, i.e., the HSP's conditional autocorrelation < 0.5 [40] or, equivalently, SBR > 6.5 [41], can ensure the rationality of the approximation. We list the references reporting a quality factor  $Q \geq 0.01$  in Table I. All of the references' biphoton sources comply with the single-photon criterion. These biphoton sources, which utilized different generation processes in various media or platforms, have revealed that a higher ESB (or SBR) consistently results in a lower SBR (or ESB). An interesting trade-off is that solid-state systems offer higher SBR values with narrower temporal widths, while atomic systems provide longer temporal widths but lower SBR values. This trade-off also occurs between SBR and the generation rate. Equation (1) explicitly encodes both trade-offs. Note that we omit Ref. [7] in the table, because its biphoton source operating in the pulse mode had a Q value, which, to the best of our knowledge, exceeds the physical bounds of this metric.

can ensure that Q has an upper limit and indicates how closely the source approaches an ideal noise-free one.

#### III. EXPERIMENTAL SETUP

We generated biphotons via the SFWM process with a paraffin-coated cylindrical glass vapor cell filled with isotopically enriched <sup>87</sup>Rb atoms. The cell, with a length of 75 mm and a diameter of 25.4 mm, was maintained at a temperature of approximately 48 °C. Figure 1 depicts the relevant energy levels and optical transitions in the experiment, where states  $|1\rangle$ ,  $|2\rangle$ ,  $|3\rangle$ , and  $|4\rangle$  represent  $|5S_{1/2}, F = 2\rangle$ ,  $|5S_{1/2}, F = 1\rangle$ ,  $|5P_{1/2}, F = 2\rangle$ , and  $|5P_{3/2}, F = 2\rangle$ , respectively. The frequency separation between ground states  $|1\rangle$  and  $|2\rangle$  is approximately 6.8 GHz, while excited states  $|3\rangle$  and  $|4\rangle$  have the spontaneous decay rate,  $\Gamma$ , of about  $2\pi \times 6$  MHz. To prepare the population in the  $|1\rangle$  ground state, we applied a hyperfine optical pumping (HOP) field in the form of a donut-shaped beam, which depleted the population in  $|2\rangle$  while minimizing disturbance to the SFWM interaction region. Throughout the study, the optical density (OD), denoted by  $\alpha$  in Eqs. (B2)-(B4), was about 500 [37].

The pump and coupling beams came from two external-cavity diode lasers (Toptica DL DLC pro) of 780 and 795 nm, respectively. We aligned them to propagate in the same direction as the collection direction of the signal and probe photons. The two laser beams completely overlapped within the vapor cell. This all-copropagating configuration ensured the phase match in the SFWM process and significantly reduced the ground-state decoherence rate caused by Doppler broadening. The pump and coupling fields were linearly polarized with the p and s polarizations, respectively. We detected the signal and probe

TABLE I: Biphoton sources with quality factors larger than 0.01.

Reference	Generation	Platform	ESB	SBR	Quality	
	Rate		$(pairs/s) \cdot \mu s$		Factor	
This work	SFWM	hot atoms	$(9.8\pm0.4)\times10^{4*}$	$6.9 \pm 0.1$	$0.68 \pm 0.02$	
[1]	SPDC	nonlinear crystal	54	$7.0{\times}10^3$	0.38	
[12]	SPDC	waveguide	310	670	0.21	
[2]	SPDC	nonlinear crystal	25	$7.9{\times}10^3$	0.20	
[16]	SFWM	micro-resonator	10	$1.4{\times}10^4$	0.14	
[6]	SPDC	nonlinear crystal	$9.8 \times 10^{3}$	13	0.13	
[32]	SFWM	hot atoms	$5.1 \times 10^{3}$	23	0.12	
[33]	SFWM	hot atoms	$1.8 \times 10^{3}$	42	0.076	
[17]	SFWM	micro-resonator	720	100	0.072	
[3]	SPDC	nonlinear crystal	$1.6 \times 10^{3}$	41	0.066	
[13]	SPDC	waveguide	1.4	$4.0{\times}10^4$	0.056	
[19]	SFMW	micro-resonator	390	77	0.030	
[18]	SFWM	micro-resonator	40	760	0.030	
[20]	SFWM	micro-resonator	15	$1.5{\times}10^3$	0.023	
[21]	SFMW	micro-resonator	52	420	0.022	
[11]	SPDC	micro-resonator	47	260	0.012	
[4]	SPDC	nonlinear crystal	42	290	0.012	
[5]	SPDC	nonlinear crystal	19	540	0.010	
[28]	pulsed SFWM	cold atoms	$38 \ (1.9^{\dagger})$	$1.5 \times 10^{4}$	0.57	
[22]	pulsed SFWM	cold atoms	$1.6 \times 10^4 (62^{\dagger})$	13	0.21	
[24]	pulsed SFWM	cold atoms	$7.8{ imes}10^3~(780^\dagger)$	22	0.17	
[26]	pulsed SFWM	cold atoms	$2.6{\times}10^{3}\ (260^{\dagger})$	44	0.11	
[27]	pulsed SFWM	cold atoms	$1.9{\times}10^3(15^\dagger)$	40	0.076	
[23]	pulsed SFWM	cold atoms	$2.8 \times 10^3 (140^{\dagger})$	20	0.056	
[25]	pulsed SFWM	cold atoms	$2.2{ imes}10^3~(220^\dagger)$	24	0.053	

<sup>\*</sup>The value refers to the biphotons collected in polarization-maintained optical fibers.

photons in the s- and p-polarization directions, using two single-photon counting modules (SPCMs) of Excelitas SPCM-AQRH-13-FC with the dark count rates of about 200 counts/s.

To eliminate the leakages of the pump and coupling laser fields to the SPCMs, we used polarization filters (Thorlabs GTH10M-B) and etalon filters (Quantaser FPE002). These filters suppressed the laser fields by more than 130 dB, so the pump's and coupling's leakages

<sup>&</sup>lt;sup>†</sup>The average value of ESB, calculated considering the duty cycle, is shown in each parentheses.

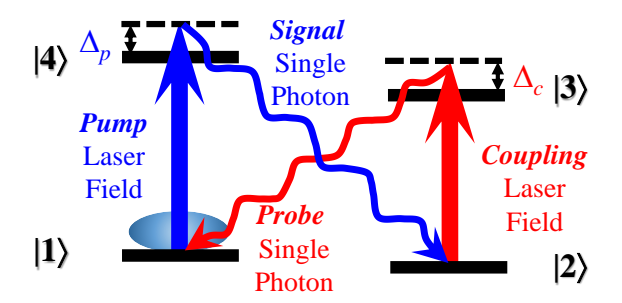


FIG. 1: The double- $\Lambda$  transition scheme for the biphoton generation used in this work. We applied the pump and coupling fields to hot atomic vapor and produced the signal and probe photons. The pump field and signal photon (the coupling field and probe photon) form the first (the second) two-photon Raman transition with a one-photon detuning of  $\Delta_p$  ( $\Delta_c$ ).

were about 19 and 5 counts/s/mW, respectively. Two polarization-maintaining optical fibers (PMFs) of Thorlabs P3-780PM-FC-2 collected the signal and probe photons. They also collected 75% and 69% of the pump and coupling beams. We do not include the PMFs' collection efficiencies when deriving a generation rate from an SPCM detection rate.

The overall detection efficiencies, including the SPCM quantum efficiency, etalon and polarization filter transmittances, and other optical losses but excluding the PMFs' collection efficiencies, were  $D_s = (13\pm1)\%$  for the signal photons and  $D_p = (9.4\pm0.5)\%$  for the probe photons. We divided the biphoton detection rate, i.e., coincidence count per second, by the product of  $D_s$  and  $D_p$  to obtain the biphoton generation rate  $R_b$ . Furthermore, we divided the signal (probe) photon detection rate by  $D_s$  ( $D_p$ ) to obtain the signal (probe) photon generation rate  $R_s$  ( $R_p$ ). The signal (probe) heralding probability  $h_s$  ( $h_p$ ) is equal to the ratio of  $R_b$  to  $R_s$  ( $R_b$  to  $R_p$ ). References [36, 37] provide more experimental details.

#### IV. RESULTS AND DISCUSSION

The pump and coupling laser fields influence the performances, e.g., the generation rate, temporal width, and background photon rate, of the double- $\Lambda$  SFWM biphoton source, as indicated by the biphoton generation theory in Appendix B [44, 45] and demonstrated by our previous works in Refs. [32, 37, 46, 47]. We systematically studied how the powers and detunings of the pump and coupling fields affect the signal's and probe's heralding probabilities  $h_s$  and  $h_p$ . Figure 2(a) [3(a)] shows  $h_s$  and  $h_p$  as functions of the pump (coupling)

power, and Fig. 2(b) [3(b)] shows those as functions of the pump (coupling) detuning, while all the other experimental parameters among the pump power and detuning, and the coupling power and detuning were maintained the same. In the figures, the red (blue) circles and squares are the experimental data of  $h_s$  ( $h_p$ ), and the red (blue) lines are the corresponding theoretical predictions.

We first studied  $h_s$  as a function of the pump power, i.e., proportional to the Rabi frequency squared or  $\Omega_p^2$ , and the pump detuning  $\Delta_p$  as shown by Figs. 2(a) and 2(b), respectively. The red circles and squares represent the experimental data, and the red lines are the theoretical predictions based on Eq. (C1) illustrated in Appendix C. In the two figures, the overall behaviors of  $h_s$  of the experimental data agree with those of the predictions, except for the data point of  $\Delta_p = 1.4$  GHz in Fig. 2(b). We discuss this data point in Appendix E, which can reveal the tendency of decreasing  $h_s$  as  $\Delta_p$  gets small. The remaining data points reveal that  $h_s$  varied very little with the pump power and detuning. We will explain the behavior of  $h_s$  in Appendix C.

We further investigated the probe's heralding probability  $h_p$  as a function of the pump power and  $\Delta_p$  as shown by Figs. 2(a) and 2(b), respectively. The experimental data or the blue circles and squares reveal that  $h_p$  increased with the pump transition rate, i.e., increased and decreased with the pump power and  $\Delta_p$ , respectively. They are consistent with the theoretical predictions shown by the blue lines in the figures. We will explain the behavior of  $h_p$  in Appendix D.

The effect on  $h_s$  as well as  $h_p$  by tuning the pump power in Fig. 2(a) is equivalent to that by tuning  $\Delta_p$  in Fig. 2(b). The equivalence originates from the roles of the pump power ( $\propto \Omega_p^2$ ) and  $\Delta_p$  in the two-photon correlation function or Eq. (B1), which determines  $R_b$ . At a large  $\Delta_p$ , one can factor out both  $\Omega_p$  and  $\Delta_p$  from the integral in Eq. (B2) and also from that in Eq. (B1). Consequently,  $R_b$  is linearly proportional to  $\Omega_p^2/\Delta_p^2$  and the proportionality depends on neither  $\Omega_p$  nor  $\Delta_p$ . In Appendix E, Figs. 6(a) and 6(b) demonstrate the equivalence.

We next studied the signal's heralding probability  $h_s$  as a function of the coupling power, i.e., proportional to the Rabi frequency squared or  $\Omega_c^2$ , and the coupling detuning  $\Delta_c$  as shown by Figs. 3(a) and 3(b), respectively. The overall trends of the experimental data (red circles and squares) agree with those of the theoretical predictions (red lines). The data revealed that as compared with  $h_p$  which will be discussed later,  $h_s$  slightly varied with the

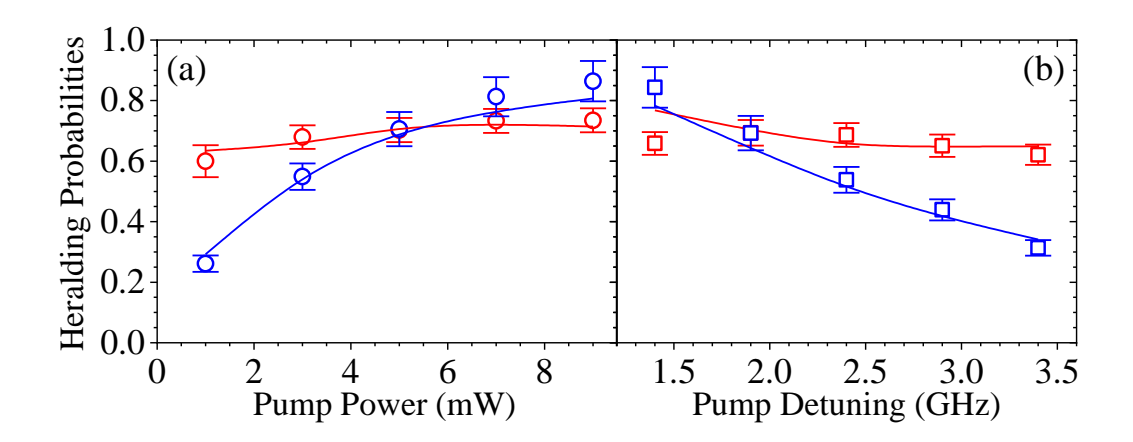


FIG. 2: The signal's and probe's heralding probabilities  $h_s$  and  $h_p$  are shown as functions of the pump (a) power and (b) detuning. Red (and blue) circles or squares are the experimental data with the signal (and probe) photons to herald coincidence counts. Each line represents the theoretical prediction with a proportionality matching the count rate in theory to that in measurement. The coupling power and detuning were 17 mW and 1.00 GHz in all the measurements. The pump detuning was 2.90 GHz in (a), and the pump power was 2 mW in (b). In the theoretical calculation, we used  $\alpha$  (OD) = 500,  $\Omega_c = 12\Gamma$ ,  $\Omega_p = 2.8\Gamma \times \sqrt{\text{pump power in mW}}$ , b = 0.375, and the various values of  $\gamma$ , which ranged  $0.0072\Gamma \sim 0.020\Gamma$  in (a) and  $0.0067\Gamma \sim 0.019\Gamma$  in (b). These calculation parameters can be found in Eqs. (B2)-(B4) and their determination methods are described in Appendix B.

coupling power or  $\Delta_c$  and had an optimum value against it. We will explain behavior of  $h_s$  in Appendix C.

We further investigated the probe's heralding probability  $h_p$  as a function of the coupling power ( $\propto \Omega_c^2$ ) and  $\Delta_c$  as shown by Figs. 3(a) and 3(b), respectively. The overall trends of the experimental data represented by the blue circles and squares are consistent with those of the theoretical predictions represented by the blue lines. The data revealed that  $h_p$  significantly decreased (increased) with the coupling power ( $\Delta_c$ ). We will explain the behavior of  $h_p$  in Appendix D.

After knowing how the powers and detunings of the pump and coupling fields affect the heralding probabilities  $h_s$  and  $h_p$ , we searched for the maximum of the pairing probability, i.e., the product of  $h_s$  and  $h_p$ . The four-dimensional search was in the volume formed by the x-axis ranges in Figs. 2 and 3. The step size precision of the detunings was 0.5 GHz, and those of the pump and coupling powers were as small as 0.5 and 1 mW, respectively.

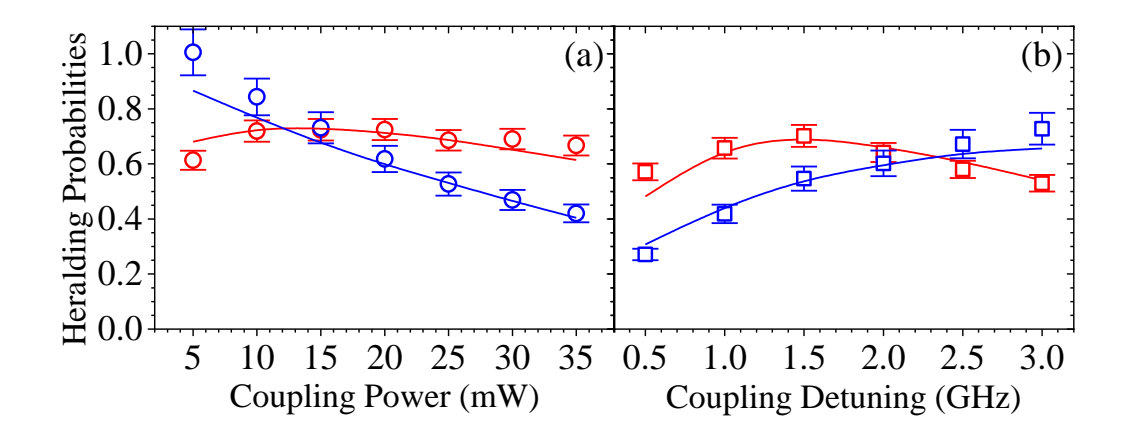


FIG. 3: The signal's and probe's heralding probabilities  $h_s$  and  $h_p$  are shown as functions of the coupling (a) power and (b) detuning. Red (and blue) circles or squares are the experimental data with the signal (and probe) photons to herald coincidence counts. Each line represents the theoretical prediction with a proportionality matching the count rate in theory to that in measurement. The pump power and detuning were 2 mW and 1.90 GHz in all the measurements. The coupling detuning was 1.00 GHz in (a), and the coupling power was 35 mW in (b). In the theoretical calculation, we used  $\alpha$  (OD) = 500,  $\Omega_c = 3.0\Gamma \times \sqrt{\text{coupling power in mW}}$ ,  $\Omega_p = 4.0\Gamma$ , b = 0.375 in (a) and 0.315 in (b), and the various values of  $\gamma$ , which ranged  $0.0075\Gamma \sim 0.045\Gamma$  in (a) and  $0.0089\Gamma \sim 0.011\Gamma$  in (b).

We maintained biphotons' peak cross-correlation > 7.5 [41], i.e., the single photon criterion that the conditional auto-correlation < 0.5 [40]. The maximum pairing probability was  $0.81\pm0.02$ , where the corresponding  $h_s$  and  $h_p$  were about 0.83 and 0.98.

We present the biphoton wave packet or two-photon correlation function, i.e., the coincidence count as a function of the probe photon's delay time upon the signal photon's heralding, at the highest pairing probability in Fig. 4. The experimental data reveal that the biphoton source had a generation rate of  $(7.5\pm0.2)\times10^5$  pairs/s as well as a temporal FWHM of  $131\pm3$  ns, corresponding to an ESB of  $9.8\times10^4$  (pairs/s)· $\mu$ s, and an SBR of  $6.9\pm0.1$ . Based on Eq. (1), the quality factor of 0.68 and pairing probability of 0.81 agreed well. We calculated the two-photon correlation function  $G^{(2)}(\tau)$  in Eq. (B1) with the calculation parameters, which were determined by the methods described in Appendix B and consistent with the calculation parameters used in Figs. 2 and 3. The theoretical prediction is in good agreement with the experimental data. In the inset of Fig. 4, the green line is the frequency spectrum of  $G^{(2)}(\tau)$  and shows asymmetry concerning its peak. We utilized a

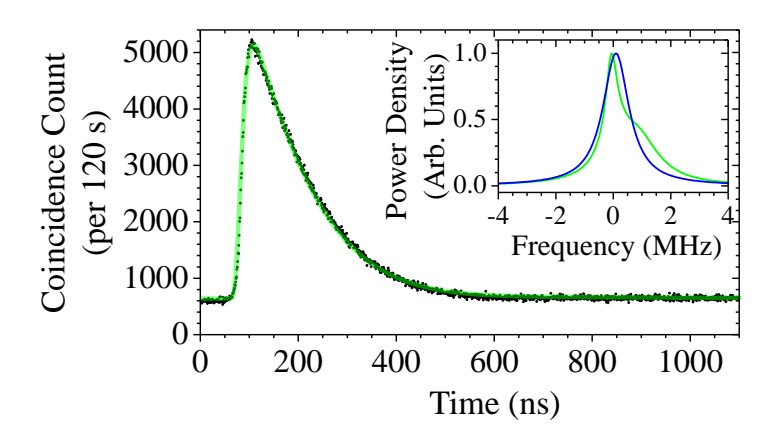


FIG. 4: Biphoton wave packet or two-photon correlation function, i.e., coincidence count as a function of the delay time of the probe photon upon the signal photon's heralding. Black dots are the experimental data with the highest quality factor achieved in this work, and the green line is the theoretical prediction. The pump and coupling powers (detunings) were 5.5 and 17 mW (1.90 and 1.00 GHz), respectively. The OD of the hot atomic vapor was about 500. With the same experimental condition, several measurements on different days reveal that the biphotons, collected in the polarization-maintained optical fibers, had a generation rate of  $(7.5\pm0.2)\times10^5$  pairs/s, a temporal FWHM of  $131\pm3$  ns, and an SBR of  $6.9\pm0.1$ . The measurements also show that the signal's and probe's heralding probabilities were  $0.83\pm0.02$  and  $0.98\pm0.02$ . Thus, the above-quoted uncertainties include the day-to-day fluctuations. In the inset, the green line represents the theoretical prediction's frequency spectrum with a FWHM of  $0.94\pm0.03$  MHz, and the blue line is the best fit of a Lorentzian function with a FWHM of  $1.07\pm0.03$  MHz. We used  $\alpha = 500$ ,  $\Omega_c = 12\Gamma$ ,  $\gamma = 0.012\Gamma$ , and b = 0.375 in the theoretical calculation.

Lorentzian function to fit the spectrum. The blue line represents the best fit, which had a FWHM slightly larger than the green line's FWHM. Due to the asymmetry in the green line, the blue line's FWHM determined the biphoton linewidth. Hence, the biphoton generation rate divided by linewidth indicates an SB of  $(7.0\pm0.3)\times10^5$  pairs/s/MHz. The quality factor and SB here reach 81% of the fundamental limit. They are also the highest records among all kinds of the heralded single photon sources.

We verified the relation between the quality factor Q and the pairing probability P as shown in Eq. (1) in Fig. 5(a). The biphoton generation rate,  $R_b$ , the biphoton wave packets' SBR and temporal FWHM,  $\Delta \tau$ , and the heralding probabilities,  $h_s$  and  $h_p$ , were measured.

The product of  $R_b$  and  $\Delta \tau$  gave the measured ESB, and that of ESB and SBR resulted in Q. The product of  $h_s$  and  $h_s$  resulted in P. Figure 5(a) shows Q as a function of P. The experimental data reveal that the quality factor is linearly proportional to the pairing probability.

The black straight line with the zero intercept in Fig. 5(a) represents the best fit of the data. Due to the differences in the biphoton temporal profiles under various experimental conditions, some data points significantly deviate from the black line. To account for these differences, we calculated the constant C shown in Eq. (1) based on each biphoton temporal profile. We plotted the normalized quality factor, i.e., Q/C, as a function of P in Fig. 5(b). The straight line with a slope 1 in the figure represents the theoretical prediction of  $Q = C \times P$ . All the experimental data points well align with the theoretical prediction, verifying the relation between the quality factor, i.e., the product of ESB and SBR, and the pairing probability, i.e., the product of the herding probabilities  $h_s$  and  $h_p$ , shown in Eq. (1). Note that the detection efficiencies  $D_s$  and  $D_p$  do not influence the verification of the relation  $Q = C \times P$  presented in Fig. 5(b). Please see the last paragraph in Appendix A for details.

We describe several references reporting significant values of the biphoton wave packet's ESB-and-SBR product in the next two paragraphs and summarize them in Table I. These references' biphoton sources comply with the single-photon criterion, i.e., the conditional auto-correlation of heralded photons is less than 0.5 or, equivalently, SBR > 6.5 [40, 41].

In each of Refs. [22–28], the authors employed laser-cooled atoms to generate biphotons via the SFWM process. Their results typically showed the biphoton wave packets with long temporal widths due to low decoherence rates in the cold-atom systems. Several of these references can achieve the  $\Delta\tau$  exceeding 500 ns. The cold-atom source operates in the pulse mode with a low duty cycle, i.e., in each period, the biphoton generation occupies a small portion of time, and the cooling and trapping of atoms take the remaining time. Consequently, the average values of  $R_b$  and ESB of a cold-atom source are low. The peak ESBs of these references ranged from 38 to  $1.6 \times 10^4$  (pairs/s)· $\mu$ s, while the corresponding SBRs were between  $1.5 \times 10^4$  and 13, respectively. In each of Refs. [32, 33], the authors employed hot atomic vapor to generate biphotons via the SFWM process. The hot-atom sources typically had shorter temporal widths yet greater generation rates than the coldatom sources. The continuous-wave (CW) ESB of a hot-atom source usually surpasses the average ESB of a cold-atom one. Moreover, the CW ESB in this work even surpassed the

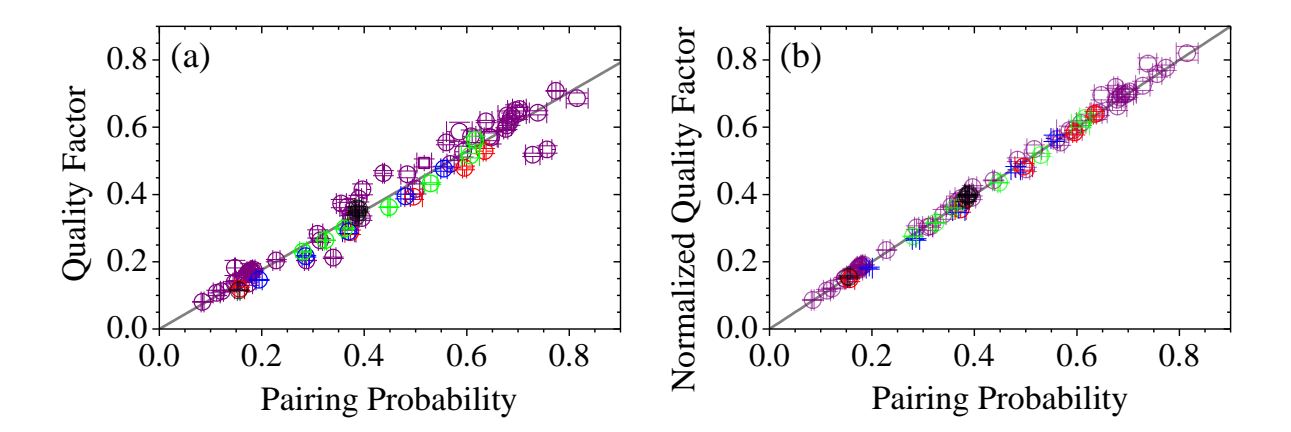


FIG. 5: (a) The quality factor, Q, and (b) the normalized quality factor, Q/C, as functions of the pairing probability, P. The definitions of Q, C, and P can be found in Eqs. (1)-(3). Red, blue, green, and black circles are the experimental data relating to Figs. 2(a), 2(b), 3(a), and 3(b), and purple ones are those during the search for the result in Fig. 4, where in the measurements the pump power ranged between 1 and 11 mW, the pump detuning changed from 1.4 to 3.4 GHz, the coupling power ranged between 3 and 36 mW, and the coupling detuning changed from 0 to 3.0 GHz. The straight line in (a) [or (b)] is the best fit (or theoretical prediction) with a slope of 0.92 (or 1).

best value of the peak ESBs of the cold-atom biphoton sources [22–28]. Across these prior and present works, the reported ESBs ranged from  $1.8\times10^3$  to  $9.8\times10^4$  (pairs/s)· $\mu$ s, while the corresponding SBRs were between 42 and 6.9, respectively.

In each of Refs. [11–13, 16–21], the authors fabricated a micro-resonator or waveguide, which enhances the nonlinear light-matter interaction, on a chip. They applied a pump laser field to the micro-resonator or waveguide and generated the biphotons via the SPDC or SFWM process. These sources have the benefits of compact form and low pump laser power. The reported ESBs in these references ranged from 1.4 to 720 (pairs/s)· $\mu$ s, while the corresponding SBRs were between  $4.0\times10^4$  and 77, respectively. In each of Refs. [1–6], the authors used a nonlinear crystal and a pump laser field to generate biphotons via the SPDC process. They typically installed an optical cavity to narrow the biphoton linewidth or prolong its temporal width effectively. However, the resonance frequency of the optical cavity is sensitive to the temperature, and its linewidth is not tunable. In these references, the reported ESBs ranged from 19 to  $9.8\times10^3$  (pairs/s)· $\mu$ s, while the corresponding SBRs were between  $7.9\times10^3$  and 13, respectively.

We derived Eq. (1) based on the fundamental theory without utilizing any device- or system-dependent assumption. Although the study presented in Fig. 5 was carried out with the hot-atom double- $\Lambda$  SFWM biphoton source, Eq. (1) is also valid for the biphoton sources in different platforms with the SPDC or SFWM process. Only a few references revealed the data of  $h_s$  and  $h_p$  of their biphoton sources, and the Q and P values of these references satisfied Eq. (1) [16, 17]. Although Table I lists only the Q values, the corresponding P value of each reference in the table can be derived from P = Q/C. The result shown in Fig. 4 has the highest P value in the table, indicating that our hot-atom biphoton source is the most similar to an ideal no-noise source.

#### V. CONCLUSION

To characterize the performance of a biphoton source in terms of spectral brightness (SB) and signal-to-background ratio (SBR) altogether, we define a new quantity, the quality factor (Q), as the product of effective SB, i.e., ESB, and SBR. Equation (1) shows that  $Q = C \times P$ , where P is the product of the heralding probabilites  $h_s$  and  $h_p$ , whose definitions are shown in Table II, and the proportionality C depends only on the biphoton wave packet's shape. Since the ESB or SB is given by the biphoton generation rate  $R_b$  times the biphoton temporal width or divided by the biphoton spectral linewidth, respectively, an ESB is smaller than its corresponding SB by a factor of the order of  $2\pi$ . The simple expression of  $Q = C \times P$  reveals that  $Q \leq 1$  and Q reaches its maximum at P = 1 as the examples in Table III. A biphoton source with a higher Q value is closer to the ideal noise-free one and contains fewer noise photons.

The underlying physics of  $Q = C \times P$  is depicted as follows: With an ideal noise-free biphoton source, i.e., P = 1 or Q = C, a more significant generation rate, temporal width, or their product (ESB or SB) increases the overlap probability between biphoton pairs and degrades SBR, and similarly a more significant SBR is achieved at the cost of decreasing ESB or SB. With a non-ideal biphoton source, i.e., P < 1, in which noise can be uncorrelated signal and probe photons, fluorescence photons, laser leakages, etc., the degradation is more severe, i.e, equivalently Q < C. We systematically studied the biphotons' Q, P, and C with a hot-atom SFWM source. The experimental data presented in Fig. 5(b) precisely verify the  $Q = C \times P$  formula.

In this work, we optimized the P value to  $81\pm0.02\%$  and achieved the Q value of  $68\pm2\%$ .

The biphoton source had a generation rate of  $(7.5\pm0.2)\times10^5$  pairs/s and a spectral linewidth

of  $1.07\pm0.03$  MHz, corresponding to an SB of  $(7.0\pm0.3)\times10^5$  pairs/s/MHz, at an SBR of

 $6.9\pm0.1$  as shown in Fig. 4. The quality factor Q and its SB are the highest records among

all biphoton sources with different generation processes and across various media, which

complied with the single photon criterion. This result marks a significant milestone in the

development of biphoton sources. Our study paves the way for advanced designs in high-

performance quantum light applications.

Data availability statement

All data that support the findings of this study are included within the article.

Acknowledgments

IAY thanks Dr. Thorsten Peters for fruitful discussion.

Data availability

Data underlying the results presented in this paper are not publicly available at this time

but may be obtained from the authors upon reasonable request.

**Funding** 

National Science and Technology Council, Taiwan (112-2112-M-007-020-MY3, 114-2119-M-

007-012).

Conflict of interest

The authors declare no conflicts of interest.

15

#### Appendix A: Relation between the quality factor and pairing probability

Equation (1) shows the relation between the quality factor Q and pairing probability P, i.e.,  $Q = C \times P$  where C is a dimensionless proportionality depending only on the biphoton wave packet's shape. References [11, 48–50] showed formulas that relate a coincidence-to-accidental ratio (CAR) to the corresponding biphoton generation rate, where CAR is the number ratio of coincidence counts to accidental counts within the time window for recording the heralded photon's arrival. Since those formulas contain no information about the biphoton temporal width, they do not reveal the underlying physics that the fundamental limit of Q is due to the overlap between biphoton wave packets. Considering the biphoton temporal width, we derive  $Q = C \times P$  here.

Table II lists the mathematical symbols frequently referred to in the derivation or main text. In addition,  $\tau_0$  and  $\Delta \tau$  represent the peak position and temporal FWHM of the biphoton wave packet,  $\Delta t_{\rm bin}$  is the time bin width, and  $\langle N_c \rangle$  and  $\langle N_{unc} \rangle$  denote the averages of the correlated and uncorrelated photon numbers per time bin per heralding event, respectively.

We first illustrate a simple case of the square-pulse biphoton wave packet with a temporal width of  $\Delta \tau$ . The SBR,  $r_{SB}$ , is given by the ratio of correlated to uncorrelated photon numbers with the heralding photons, i.e.,

$$r_{SB} = \frac{\langle N_c(\tau_0) \rangle}{\langle N_{unc} \rangle} = \frac{h_s \times (\Delta t_{\text{bin}}/\Delta \tau) + (1 - h_s) \times 0}{R_p \Delta t_{\text{bin}}}.$$
 (A1)

In the numerator of the above equation,  $h_s \times (\Delta t_{\rm bin}/\Delta \tau)$  means that each photon in the heralding channel has a probability of  $h_s$  to pair with its counterpart or heralded photon, and the counterpart photon has a probability of  $\Delta t_{\rm bin}/\Delta \tau$  to appear in the time bin centering around  $\tau_0$  due to the square pulse. Naturally, each photon in the heralding channel has a probability of  $1 - h_s$  without any counterpart or does not contribute to  $\langle N_c(\tau_0) \rangle$ . Thus,  $h_s$  is the signal's heralding probability, i.e.,  $R_b/R_s$ . In the numerator of the above equation, we do not specify the time due to the random appearance in the heralded channel of the photons uncorrelated with a given heralding photon, and  $R_p$  is the photon rate in the heralded channel and relates to the biphoton generation rate by  $R_b = h_p R_p$  where  $h_p$  is the probe's heralding probability. The above equation now becomes

$$r_{SB} = \frac{h_s/\Delta\tau}{R_b/h_p} = \frac{h_s h_p}{R_b \Delta\tau} \tag{A2}$$

TABLE II: Table of mathematical symbols.

Name	Symbol	Definition
Generation Rates	$R_b, R_s, R_p$	Generation rates of biphotons, photons in the heralding (or signal detection) channel, and those in the heralded (or probe detection) channel, respectively.
Signal's and Probe's Heralding Probabilities	$h_s, h_p$	Ratios of $R_b$ to $R_s$ and $R_b$ to $R_p$ , respectively.
Biphoton's Pairing Probability	P	Product of $h_s$ and $h_p$ .
Temporal FWHM	$\Delta  au$	Full width at half maximum of the biphoton wave packet's temporal profile.
Signal-to-Background Ratio (SBR)	$r_{SB}$	Ratio of the correlated counts at the biphoton wave packet's peak to the background counts.
Quality Factor	Q	Product of effective spectral brightness, $R_b \Delta \tau$ , and $r_{SB}$ .

or, equivalently,

$$Q \equiv r_{SB}(R_b \Delta \tau) = h_s h_p \equiv P. \tag{A3}$$

All the above symbols' definitions are shown in Table II. Thus, Q = P for the square-pulse biphoton wave packet.

Following the above derivation, we now consider the biphoton wave packet with an arbitrary pulse shape. The term of  $\Delta t_{\rm bin}/\Delta \tau$  in the numerator of Eq. (A1) is revised to  $C \times (\Delta t_{\rm bin}/\Delta \tau)$ , where

$$C \equiv \left[ \frac{f(\tau_0)}{\int_{-\infty}^{\infty} f(\tau) d\tau} \right] \Delta \tau \tag{A4}$$

and  $f(\tau)$  is the biphoton wave packet's temporal profile. The expression in the brackets represents the peak value of a normalized biphoton wave packet, where the normalization requires the probability of the entire wave packet being 1. The variation of the C value is merely due to different temporal shapes resulting in different peak values due to the normalization. Consequently, we have obtained

$$Q = C \times P. \tag{A5}$$

In the derivation, we utilize the condition that the time bin width is much shorter than the biphoton temporal width, i.e.,  $\Delta t_{\rm bin} \ll \Delta \tau$ , and the approximation of one heralded photon

TABLE III: The quality factor's limit, i.e., Q, at the pairing probability P equal to 1.

Function Name	Functional Form	Limit of $Q$
Single Exponential	$(1/\tau_w) \exp[-(\tau - \tau_0)/\tau_w] \ (\tau \ge \tau_0)$ and $0 \ (\tau < \tau_0)$	$\ln 2\approx 0.69$
Double Exponential	$(1/2\tau_w)\exp[- \tau-\tau_0 /\tau_w]$	$\ln 2\approx 0.69$
Gaussian	$(1/\sqrt{\pi}\tau_w)\exp[-(\tau-\tau_0)^2/\tau_w^2]$	$2\sqrt{\ln 2/\pi}\approx 0.94$
Square	$1/\tau_w \ (\tau_0 \le \tau \le \tau_0 + \tau_w)$ and 0 (otherwise)	1.0

per successful heralding event, i.e.,  $h_s \times (\Delta t_{\rm bin}/\Delta \tau)$  for square pulses in Eq. (A1) or  $h_s \times C(\Delta t_{\rm bin}/\Delta \tau)$  for arbitrary pulses. The single-photon criterion, i.e., the HSP's conditional auto-correlation,  $g_c^{(2)}(0)$ , < 0.5 [40], can ensure the rationality of the approximation. Hence, the above equation is valid for all biphoton sources, regardless of their generation processes or platforms, as long as they comply with the single-photon criterion. Table III shows the values of C of given temporal shapes or, equivalently, the maximum values of C at C a

The relation of  $Q = C \times P$  in Eq. (A5) does not depend on the detection efficiencies  $D_s$  and  $D_p$  of photons in the heralding and heralded channels. One multiplies  $D_s D_p$  to both sides of the equation and obtains

$$(R_b D_s D_p) \Delta \tau \, r_{SB} = C \times (h_s D_p)(h_p D_s) \tag{A6}$$

or, equivalently,

$$R_d \,\Delta \tau \, r_{SB} = C \times e_s e_p,\tag{A7}$$

where  $R_d$  is the biphoton detection rate or coincidence count rate, and  $e_s$  ( $e_p$ ) is the heralding efficiency by using the detected signal (probe) photons to herald detecting coincidence counts. The biphoton source's  $R_d$ ,  $e_s$ , and  $e_p$  are the directly measured quantities. Both of  $\Delta \tau$  and  $r_{SB}$  are independent of  $D_s$  and  $D_p$ . Therefore, the detection efficiencies do not influence the verification of  $Q = C \times P$  presented in Fig. 5(b).

## Appendix B: Theoretical predicitons of the two-photon correlation function and biphoton generation rate

We use the biphoton generation rate in the theoretical predictions of the signal's and probe's heralding probabilities and illustrate it in this appendix. The biphoton generation rate is calculated from the two-photon correlation function,  $G^{(2)}(\tau)$ , or biphoton wave packet

[44, 45]. Reference [37] provides the study on  $G^{(2)}(\tau)$  based on the double- $\Lambda$  SFWM biphoton source using a Doppler-broadened atomic medium. For the completeness of this article, but without illustration in depth, we list the formula of  $G^{(2)}(\tau)$  below:

$$G^{(2)}(\tau) = \left| \int_{-\infty}^{\infty} d\delta \frac{e^{-i\delta\tau}}{2\pi} \bar{\kappa}(\delta) \operatorname{sinc}[\bar{\rho}_c(\delta) + \bar{\rho}_m(\delta)] e^{i[\bar{\rho}_c(\delta) + \bar{\rho}_m(\delta)]} B(\delta) \right|^2, \tag{B1}$$

where  $\delta$  denotes the two-photon detuning,  $\bar{\kappa}(\delta)$  is proportional to the cross-susceptibility between the signal and probe photons,  $\bar{\rho}_c(\delta)$  and  $\bar{\rho}_m(\delta)$  are proportional to the probe photon self-susceptibilities induced by the atoms exhibiting the electromagnetically induced transparency (EIT) effect and those without the EIT effect or the impurity atoms, respectively, and  $B(\delta)$  represents the combined frequency spectrum of the probe and signal etalons. The four functions of  $\delta$  are defined as follows:

$$\bar{\kappa}(\delta) = \frac{(1-b)\alpha}{4} \int_{-\infty}^{\infty} d\omega_D \left[ \frac{e^{-\omega_D^2/\Gamma_D^2}}{\sqrt{\pi}\Gamma_D} \frac{\Omega_p}{\Delta_p + \omega_D + i\Gamma/2} \right] \times \frac{\Omega_c \Gamma}{\Omega_c^2 - 4(\delta + i\gamma)(\delta + \Delta_c + \omega_D + i\Gamma/2)} , \tag{B2}$$

$$\bar{\rho}_c(\delta) = \frac{(1-b)\alpha}{2} \int_{-\infty}^{\infty} d\omega_D \left[ \frac{e^{-\omega_D^2/\Gamma_D^2}}{\sqrt{\pi}\Gamma_D} \frac{(\delta+i\gamma)\Gamma}{\Omega_c^2 - 4(\delta+i\gamma)(\delta+\Delta_c+\omega_D+i\Gamma/2)} \right], \tag{B3}$$

$$\bar{\rho}_m(\delta) = \frac{b\alpha}{2} \int_{-\infty}^{\infty} d\omega_D \left[ \frac{e^{-\omega_D^2/\Gamma_D^2}}{\sqrt{\pi}\Gamma_D} \frac{\Gamma}{4(\delta + \Delta_c + \omega_D + i\Gamma/2)} \right], \tag{B4}$$

$$B(\delta) = \left(\frac{1}{1 + 2i\delta/\Gamma_e}\right)^4,\tag{B5}$$

where  $\omega_D$  represents the Doppler shift due to atomic velocity,  $\alpha$  is the optical depth (OD) of the medium, b is the fraction of the impurity atoms,  $\Gamma$  ( $\approx 2\pi \times 6$  MHz in this work) is the spontaneous decay rate of the excited states,  $\Omega_p$  and  $\Omega_c$  denote the Rabi frequencies of the pump and coupling fields,  $\Delta_p$  and  $\Delta_c$  are the pump's and coupling's one-photon detuning,  $\gamma$  represents the decoherence rate in the experimental system, and  $\Gamma_e$  is the spectral FWHM of each etalon.

The biphoton generation rate,  $R_b$ , is proportional to the integral of the biphoton wave packet over the delay time given by

$$R_b \propto \int_{-\infty}^{\infty} d\tau G^{(2)}(\tau) \quad \text{or} \quad R_b = A \int_{-\infty}^{\infty} d\tau G^{(2)}(\tau),$$
 (B6)

where A is a dimensionless proportionality accounting for the ratio of the measured value of  $R_b$  to the theoretical value of  $\int_{-\infty}^{\infty} d\tau G^{(2)}(\tau)$ . The day-to-day variations of the detection

efficiencies affected A. We kept A constant to match the predictions of  $h_s$  and  $h_p$  to the experimental data in each of Figs. 2(a), 2(b), 3(a), and 3(b). The measured values of  $R_b$  revealed that A varied within  $(1.3\pm0.1)\times10^6$  between the figures.

In the calculations of  $G^{(2)}(\tau)$  and  $R_b$ , we set  $\Gamma_D = 54\Gamma$  based on the atomic vapor cell's temperature,  $\alpha = 500$  determined from the absorption spectrum of a weak laser field, and  $\Gamma_e$  (=  $2\pi \times 53.5$  MHz or  $8.9\Gamma$ ) determined by measuring the singal and probe etalons' transmission spectra. Furthermore,  $\Omega_c$ , b, and  $\gamma$  significantly influenced  $R_b$  and the biphoton temporal width  $\Delta \tau$ , and we utilized a series of experimental data of  $R_b$  and  $\Delta \tau$  as functions of the coupling detuning or power to determine their values [37]. After obtaining the ratio of  $\Omega_c^2$  to the coupling power and the value of b that best matched the predictions with a constant  $\gamma$  to the data, we slightly adjusted  $\gamma$  to make each predicted temporal profile better agree with its corresponding experimental one [47]. Since  $\Omega_p$  does not affect the temporal profile and only changes the value of A in Eq. (B6) [32], its absolute magnitude is irrelevant in this study. We estimated the value of  $\Omega_p$  with the power, beam size, and transition strength of the pump field [46, 51].

#### Appendix C: The signal's heralding probability

We first illustrate the formula for the signal's heralding probability,  $h_s$ . The photon generation rate in the signal detection channel,  $R_s$ , is proportional to the pump-signal two-photon transition rate. In addition to the biphotons' signal photons, the photons resulting in  $R_s$  also consist of the signal photons that have lost their counterparts (i.e., the uncorrelated signal photons), fluorescence photons induced by the pump field, and pump laser leakage. Nevertheless, the two latters made negligible contributions to  $R_s$  with a large one-photon detuning. The transition rate at the two-photon resonance is approximately proportional to  $(\Omega_p/2\Delta_p)^2$ , where  $\Omega_p$  and  $\Delta_p$  represent the pump Rabi frequency and detuning. Thus, we obtain

$$h_s \equiv \frac{R_b}{R_s} = \frac{R_b}{B[\Omega_n^2/(4\Delta_n^2)]},\tag{C1}$$

where B is a proportionality and has no dependence on  $P_p$ ,  $\Delta_p$ , or the coupling power or detuning, and  $R_b$  is given by Eq. (B6).

Similar to the proportionality A in  $R_b$ , we kept the value of B constant in each of Figs. 2(a), 2(b), 3(a), and 3(b). Note that A and B are not two independently adjustable

parameters in Eq. (C1), but A/B is the only one to match the overall magnitude of predictions to that of data. The best matches revealed that the values of A/B varied within  $(1.4\pm0.1)\times10^{-4}$  s<sup>-1</sup> between the figures.

We expalin the behavior of  $h_s$  versus the pump power and detuning as shown by Figs. 2(a) and 2(b) in this and the next paragraphs. The biphoton generation rate,  $R_b$ , is linearly proportional to the pump transition rate, i.e.,  $\approx \Omega_p^2/\Delta_p^2$  at large  $\Delta_p$ , as expected from the biphoton generation theory. The signal photon generation rate,  $R_s$ , is also linearly proportional to the pump transition rate due to the spontaneous Raman transition induced by the pump field and signal photon. Hence,  $h_s$  (=  $R_b/R_s$ ) varied very little with the pump power and detuning.

The slight variations of  $h_s$  versus the pump power and detuning were caused by the variation of the ground-state decoherence rate,  $\gamma$ . Since  $\gamma$  also affected a biphoton wave packet's temporal width, we utilized Eq. (B1) of Appendix B and compared the theoretical and experimental temporal profiles to determine the value of  $\gamma$  at each pump power and detuning. The red lines in Figs. 2(a) and 2(b) are the theoretical prediction of  $h_s$  calculated with the pre-determined value of  $\gamma$  and Eq. (C1). The theoretical predictions will be two horizontal lines if we make  $\gamma$  the same for all the pump powers and detunings. Therefore, as long as the pump power or detuning is the only variable in the hot-atom double- $\Lambda$  SFWM biphoton source, it does not affect the signal's heralding probability.

Regarding the behavior of  $h_s$  against the coupling power in Fig. 3(a), the FWM efficiency, i.e.,  $|\bar{\kappa}|^2$  [see Eq. (B1)], and the variation of the ground-state decoherence rate  $\gamma$  are the two main effects. The fraction involving  $\Omega_c$  in  $|\bar{\kappa}|^2$  [see Eq. (B2)] illustrates that as the term of  $\Omega_c^2$  was smaller than that of  $8\gamma\Delta_c^2/\Gamma$  in the denominator, which was the experimental situation, the biphoton generation rate  $R_b$  increases with the numerator's  $\Omega_c^2$ . Furthermore, the pre-determined value of  $\gamma$  increased with the coupling power, and a more significant  $\gamma$  resulted in a smaller  $R_b$ . The combined effect of  $|\bar{\kappa}|^2$  and  $\gamma$  results in an optimum  $R_b$  against coupling power. In Fig. 3(a), the pump power and detuning were constant, and the signal photon generation rate  $R_s$  did not change. Hence,  $h_s$  (=  $R_b/R_s$ ) slightly varied with the coupling power and had an optimum value against it.

Regarding the behavior of  $h_s$  against  $\Delta_c$  in Fig. 3(b), the non-EIT atoms and FWM efficiency,  $|\bar{\kappa}|^2$ , are the two main effects. We did not show the data point for  $\Delta_c/2\pi < 0.5$  GHz in the figure, because as  $\Delta_c$  approached zero,  $h_s$  dropped dramatically due to

the absorption of non-EIT atoms (see the study in Ref. [37]). Note that in this work, the absorption coefficient is reduced to 0.1 at  $\Delta_c/2\pi=630$  MHz. As  $\Delta_c\geq0.5$  GHz, it decreased the FWM efficiency as indicated by the term of  $\gamma^2\Delta_c^2$  in the denominator of  $|\bar{\kappa}|^2$ . Note that the pre-determined  $\gamma$  values were about the same against  $\Delta_c$ . The theoretical predictions calculated from Eq. (B1) consider all of the effects on  $R_b$ , including the above-mentioned non-EIT atoms and FWM efficiency, due to the coupling detuning. Since the pump power and detuning were constant,  $R_s$  remained the same. Thus, for  $\Delta_c/2\pi \geq 0.5$  GHz,  $h_s = (R_b/R_s)$  changed slightly compared with  $h_p$ , and the value of  $h_s$  first increased and then decreased with  $\Delta_c$ .

#### Appendix D: The probe's heralding probability

We first illustrate the formula for the probe's heralding probability,  $h_p$ . The photon generation rate in the probe detection channel,  $R_p$ , consists of two main parts. The first part is the biphoton's or correlated probe photon rate, equal to  $R_b$ . The second part is the rate of noise photons,  $R_{pn}$ , appearing without the presence of the pump field. Although we applied the hollow-cored pumping field to optically pump out of the ground state  $|2\rangle$  driven by the coupling field, a few atoms entering the SFWM interaction region still had the population in  $|2\rangle$ . These atoms and the coupling field contributed to the noise photons. Thus,  $R_p = R_b + R_{pn}$  and we obtain

$$h_p \equiv \frac{R_b}{R_p} = \frac{R_b}{R_b + R_{pp}},\tag{D1}$$

where  $R_b$  is given by Eq. (B6).

The coupling power ( $\propto \Omega_c^2$ ) and detuning ( $\Delta_c$ ) and other experimental conditions can influence  $R_{pn}$ . Since the proportionality A in  $R_b$  is already an adjustable parameter to match the overall magnitude of theoretical predictions to that of experimental data, we intend not to introduce another independently adjustable parameter in the formula of  $h_p$ . Thus,  $R_{pn}$  in Eq. (D1) is the measured value in the corresponding experimental condition.

We expalin the behavior of  $h_p$  versus the pump power and detuning as shown by Figs. 2(a) and 2(b) in this and the next paragraphs. The behavior was caused by the noise photons in the probe detection channel, which were present even in the absence of the pump field. While the biphoton generation rate  $R_b$  increases with the pump transition rate,

the noise photon rate is approximately independent of the pump transition rate. A higher pump power or  $\Delta_p$  makes the noise photons more insignificant or significant in the total photons of the probe detection channel. Consequently,  $h_p$  significantly increases (decreases) with the pump power  $(\Delta_p)$ .

To verify the above explanation, we measured the noise photon rate in the probe detection channel without the presence of the pump field. The theoretical prediction of  $h_p$  considers the measured noise photon rate. The blue lines in Figs. 2(a) and 2(b) are the theoretical predictions of  $h_p$  based on Eq. (D1). The consistency between the predictions and the data is satisfactory, clarifying that the ratio of the noise photon rate in the probe detection channel to the rate of biphotons' probe photons is the decisive factor for the probe's heralding probability in the hot-atom double- $\Lambda$  SFWM biphoton source.

In Figs. 3(a) or 3(b), the behavior of  $h_p$  significantly decreasing or increasing with the coupling power or  $\Delta_c$ , respectively, can be again explained by the noise photons in the probe detection channel. A larger coupling power ( $\Delta_c$ ) induced more (fewer) fluorescence photons, and the noise photon rate approximately linearly increased (decreased) with the coupling power ( $\Delta_c$ ). On the other hand,  $R_b$  varied slightly with the coupling power ( $\Delta_c$ ) as demonstrated by the insignificant changes of  $h_s$  against the coupling power ( $\Delta_c$ ) in the exact figure illustrated earlier. Consequently, the coupling power (detuning) in the region of the figure reduced (enhanced)  $h_p$  significantly.

### Appendix E: Equivalence between the effects on the heralding probabilities induced by the pump power and detuning

We present the experimental evidence in this appendix, clarifying that the effect on the heralding probabilities  $h_s$  and  $h_p$  induced by the pump power  $P_p$  ( $\propto \Omega_p^2$ ) is equivalent to that by the pump detuning ( $\Delta_p$ ). Figures 6(a) and 6(b) show  $h_s$  and  $h_p$  as functions of  $P_p/\Delta_p^2$ , respectively. One can either increase  $P_p$  or decrease  $\Delta_p^2$  to achieve the same values of  $h_s$  and  $h_p$ . The effects due to  $P_p$  and  $\Delta_p^2$  are equivalent.

The biphoton generation theory of the double- $\Lambda$  SFWM source in Appendix B also supports the equivalence. As long as  $\Delta_p$  is significantly greater than the natural linewidth  $\Gamma/2\pi$  ( $\approx 6$  MHz) and also the Doppler width  $\Gamma_D/2\pi$  ( $\approx 320$  MHz), one can move the term containing  $\Omega_p$  and  $\Delta_p$  in Eq. (B2) out of the inetgral or ensemble average of a Doppler-

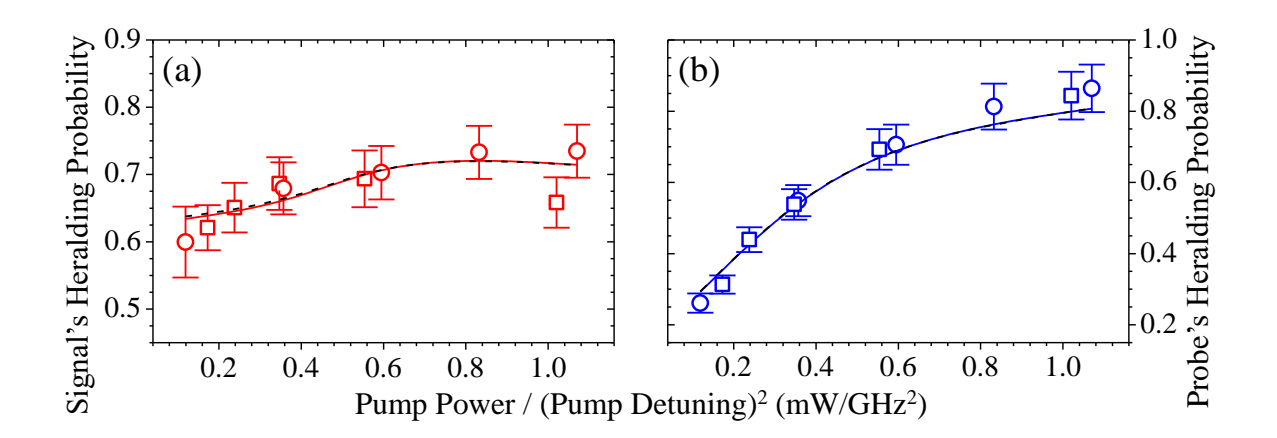


FIG. 6: (a) The signal's and (b) the probe's heralding probabilities  $h_s$  and  $h_p$  are plotted as functions of the pump power divided by the square of pump detuning. Circles are the same experimental data in Fig. 2(a), and squares are the same experimental data in Fig. 2(b). Solid red and blue lines have the same theoretical values of  $h_s$  and  $h_p$  in Fig. 2(a), respectively. We calculated the dashed black lines by factoring the pump power and detuning out of the integral in Eq. (B1).

broadened medium, i.e.,

$$\bar{\kappa}(\delta) \approx \frac{\Omega_p}{\Delta_p} \,\bar{\kappa}'(\delta),$$
 (E1)

where  $\bar{\kappa}'(\delta)$  represents the remaining part of  $\bar{\kappa}(\delta)$  that does not consist of  $\Omega_p$  and  $\Delta_p$ . Then, the two-photon correlation function in Eq. (B1) and the biphoton generation rate in Eq. (B6) become

$$G^{(2)}(\tau) \approx \frac{\Omega_p^2}{\Delta_p^2} G'^{(2)}(\tau) \text{ and } R_b \approx \frac{\Omega_p^2}{\Delta_p^2} A \int_{-\infty}^{\infty} d\tau G'^{(2)}(\tau),$$
 (E2)

where  $G'^{(2)}(\tau)$  denotes the remaining part of  $G^{(2)}(\tau)$  that does not consist of  $\Omega_p$  and  $\Delta_p$ . Thus,  $R_b$  is linearly proportional to  $\Omega_p^2/\Delta_p^2$ . Finally,  $h_s$  in Eq. (C1) and  $h_p$  in Eq. (D1) are functions of a single independent variable of  $\Omega_p^2/\Delta_p^2$  but not two independent ones of  $\Omega_p$  and  $\Delta_p$ . The nearly complete overlap between the solid and dashed lines in Figs. 6(a) and 6(b) verifies the above arguments. Hence, the effect on the heralding probabilities due to increasing the pump power and that due to decreasing the pump detuning are equivalent.

The rightmost squared data point in Fig. 6(a) significantly deviates from the theoretical prediction. This data point's  $\Delta_p/2\pi$  is 1.4 GHz. We attributed the deviation to fluorescence photons induced by the pump transition to the excited state  $|4\rangle$ . The fluorescence rate cannot be formulated by  $\Omega_p^2/(4\Delta_p^2)$ , i.e., the pump transition rate at the zero atomic velocity, when

 $\Delta_p$  is not significantly larger than the Doppler width. One needs to do the velocity average of the pump transition rate to obtain the fluorescence rate, and the average value is larger than the value of  $B\Omega_p^2/(4\Delta_p^2)$ . Furthermore, a smaller  $\Delta_p$  resulted in a higher transmission of the fluorescence photons passing through the etalons, contributing more noise photons in the signal detection channel. As  $\Delta_p$  got small, the fluorescence-induced noise photon rate became nonnegligible compared to the signal photon rate, reducing the signal's heralding probability.

- [3] Wu C-H, Wu T-Y, Yeh Y-C, Liu P-H, Chang C-H, Liu C-K, Cheng T and Chuu C-S 2017 Phys. Rev. A 96 023811
- [4] Rieländer D, Lenhard A, Mazzera M, and Riedmatten H D 2016 New J. Phys. 18, 123013
- [5] Mottola R, Buser G, Müller C, Kroh T, Ahlrichs A, Ramelow S, Benson O, Treutlein P and Wolters J 2020 Opt. Express 28 3159-3170
- [6] Kao Y-C, Huang S-H, Chang C-H, Wu C-H, Chu S-H, Jiang J, Zhang A-C, Huang S-Y, Yan J-H, Feng K-M and Chuu C-S 2023 Opt. Express 31 30239
- [7] Luo K-H, Herrmann H, Krapick S, Brecht B, Ricken R, Quiring V, Suche H, Sohler W and Silberhorn C 2015 New J. Phys. 17 073039
- [8] Tsai P-J and Chen Y-C 2018 Quantum Sci. Technol. 3 034005
- [9] Chuu C-S, Yin G Y and Harris S E 2012 Appl. Phys. Lett. **101** 051108
- [10] Sultanov V and Chekhova M 2024 ACS Photonics 11 2-6
- [11] Guo X, Zou C, Schuck C, Jung H, Cheng R and Tang H X 2016 Light Sci. Appl. 6 e16249
- [12] Zhao J, Ma C, Rüsing M and Mookherjea S 2020 Phys. Rev. Lett. 124 163603
- [13] Bock M, Lenhard A, Chunnilall C and Becher C 2016 Opt. Express 24 23992-24001
- [14] Pomarico E, Sanguinetti B, Gisin N, Thew R, Zbinden H, Schreiber G, Thomas A and Sohler W 2009 New J. Phys. 11 113042
- [15] Zhu E Y, Tang Z, Qian L, Helt L G, Liscidini M, Sipe J E, Corbari C, Canagasabey A, Ibsen

<sup>[1]</sup> Li Y-H, Zhou Z-Y, Liu S-L, Li Y, Liu S-K, Yang C, Wang S, Zhu Z, Gao W, Guo G-C and Shi B-S 2021 OSA Continuum. 4 608-620

<sup>[2]</sup> Gao M-Y, Li Y-H, Li Y, Zhou Z, Guo G-C, Zhou Z-Y and Shi B-S 2024 Phys. Rev. A. 109 033720

- M and Kazansky P G 2012 Phys. Rev. Lett. 108 213902
- [16] Ma C, Wang X, Anant V, Beyer A D, Shaw M D and Mookherjea S 2017 Opt. Express 25 32995-33006
- [17] Lu X, Jiang W C, Zhang J and Lin Q 2016 ACS Photonics 3 1626-1636
- [18] Kumar R R, Raevskaia M, Pogoretskii V, Jiao Y and Tsang H K 2019 J. Opt. 21 115201
- [19] Starling D J, Poirier J, Fanto M, Steidle J A, Tison C C, Howland G A and Preble S F 2020 Phys. Rev. Appl. 13 041005
- [20] Ma C, Wang X and Mookherjea S 2018 Opt. Express 26 22904-22915
- [21] Lu X, Li Q, Westly D A, Moille G, Singh A, Anant V and Srinivasan K 2019 Nat. Phys. 15 373-381
- [22] Shiu J-S, Liu Z-Y, Cheng C-Y, Huang Y-C, Yu I A, Chen Y-C, Chuu C-S, Li C-M, Wang S-Y and Chen Y-F 2024 Phys. Rev. Res. 6 L032001
- [23] Li J-F, Wang Y-F, Su K-Y, Liao K-Y, Zhang S-C, Yan H and Zhu S-L 2019 Chinese Phys. Lett. 36 074202
- [24] Liu C, Sun Y, Zhao L, Zhang S, Loy M M T and Du S 2014 Phys. Rev. Lett. 113 133601
- [25] Zhao L, Guo X, Liu C, Sun Y, Loy M M T and Du S 2014 Optica 1 84-88
- $[26]\,$  Han Z, Qian P, Zhou L, Chen J F and Zhang W 2015 Sci. Rep. 5 9126
- [27] Wang Y-S, Li K-B, Chang C-F, Lin T-W, Li J-Q, Hsiao S-S, Chen J-M, Lai Y-H, Chen Y-C, Chen Y-F, Chuu C-S and Yu I A 2022 APL Photonics 7 126102
- [28] Cerè A, Srivathsan B, Gulati G K, Chng B and Kurtsiefer C 2018 Phys. Rev. A. 98 023835
- [29] Farrera P, Heinze G, Albrecht B, Ho M, Chávez M, Teo C, Sangouard N and de Riedmatten H 2016 Nat. Commun. 7 13556
- [30] Chinnarasu R, Liu C-Y, Ding Y-F, Lee C-Y, Hsieh T-H, Yu I A and Chuu C-S 2020 Phys. Rev. A 101 063837
- [31] Bruns A, Hsu C-Y, Stryzhenko S, Giese E, Yatsenko L P, Yu I A, Halfmann T and Peters T 2023 Quantum Sci. Technol. 8 015002
- [32] Chen J-M, Hsu C-Y, Huang W-K, Hsiao S-S, Huang F-C, Chen Y-H, Chuu C-S, Chen Y-C, Chen Y-F and Yu I A 2022 Phys. Rev. Res. 4 023132
- [33] Craddock A N, Wang Y, Giraldo F, Sekelsky R, Flament M and Namazi M 2024 Phys. Rev. Appl. 21 034012
- [34] Jeong H, Kim H and Moon H S 2024 Adv. Quantum Technol. 7 2300108

- [35] Willis R T, Becerra F E, Orozco L A and Rolston S L 2011 Opt. Express 19 14632
- [36] Huang W-K, Kim B, Shih T-J, Hsu C-Y, Tu P-Y, Lin T-Y, Chen Y-F, Chuu C-S, and Yu I A 2025 Quantum Sci. Technol. 10 015062
- [37] Huang W-K, Lin T-Y, Tu P-Y, Chen Y-F and Yu I A 2025 arXiv:2502.06344
- [38] Jeong T and Moon H S 2020 Opt. Express 28 3985-3994
- [39] Mika J, Lachman L, Lamich T, Filip R and Slodička L 2022 npj Quantum Inf. 8 123
- [40] Grünwald, P 2019 New J. Phys. **21** 093003
- [41] Shih T-J, Huang W-K, Lin Y-M, Li K-B, Hsu C-Y, Chen J-M, Tu P-Y, Peters T, Chen Y-F and Yu I A 2024 Opt. Express 32 13657
- [42] Slattery O, Ma L, Zong K and Tang X 2019 J. Res. Natl. Inst. Stan. Technol. 124 124019
- [43] Wang Y, Jöns K D and Sun Z 2021 Appl. Phys. Rev. 8 011314
- [44] Chen J-M, Peters T, Hsieh P-H and Yu I A 2024 Adv. Quantum Technol. 7 2400138
- [45] Du S, Wen J and Rubin M H 2008 J. Opt. Soc. Am. B **25** C98
- [46] Hsu C-Y, Wang Y-S, Chen J-M, Huang F-C, Ke Y-T, Huang E K, Hung W, Chao K-L, Hsiao S-S, Chen Y-H, Chuu C-S, Chen Y-C, Chen Y-F and Yu I A 2021 Opt. Express 29 4632
- [47] Hsiao S-S, Huang W-K, Lin Y-M, Chen J-M, Hsu C-Y and Yu I A 2022 Phys. Rev. A 106 023709
- [48] Prabhakar S, Shields T, Dada A C, Ebrahim M, Taylor G G, Morozov D, Erotokritou K, Miki S, Yabuno M, Terai H, Gawith C, Kues M, Caspani L, Hadfield R H and Clerici M 2020 Sci. Adv. 6 eaay5195
- [49] Förtsch M, Schunk G, Fürst J U, Strekalov D, Gerrits T, Stevens M J, Sedlmeir F, Schwefel H G L, Nam S W, Leuchs G and Marquardt C 2015 Phys. Rev. A. 91 023812
- [50] Zhang Y, England D, Nomerotski A, Svihra P, Ferrante S, Hockett P and Sussman B 2020 Phys. Rev. A. 101 053808
- [51] Steck D A 2021 Rubidium 87 D Line Data, rev. 2.3.3 http://steck.us/alkalidata